Available online at www.sciencedirect.com
SCIENCE DIRECT®
International Journal of Heat and Mass Transfer 47 (2004) 5575–5589
International Journal of HEAT and MASS TRANSFER
www.elsevier.com/locate/ijhmt

Bubble dynamics in microchannels. Part I: single microchannel

P.C. Lee, F.G. Tseng, Chin Pan *

Department of Engineering and System Science, National Tsing Hua University, Hsinchu 30043, Taiwan, ROC

Received 9 December 2003; received in revised form 7 February 2004
Available online 17 September 2004

Abstract

The present work explores experimentally bubble dynamics in a single trapezoid microchannel with a hydraulic diameter of 41.3 μm. The fabrication process of the microchannel employs a silicon bulk micromachining and anodic bounding process. Bubble nucleation, growth, departure size, and frequency are observed using a high speed digital camera and analyzed by the Image-Pro. The results of the study indicates that the bubble nucleation in the microchannel may be predicted from the classical model with microsized cavities and the bubble typically grows with a constant rate from 0.13 to 7.08 μm/ms. Some cases demonstrate an extraordinarily high growth rate from 72.8 to 95.2 μm/ms. The size of bubble departure from the microchannel wall is found to be governed by surface tension and drag of bulk flow and may be fairly correlated by a modified form of Levy equation. The bubble frequency in the microchannel is comparable to that in an ordinary sized channel. The traditional form of frequency–departure-diameter relationship seems to be inexistent in the microchannel of this study.

Keywords: Microchannel; Bubble dynamics; Onset nucleate boiling; Boiling heat transfer

1. Introduction

Boiling heat transfer in a microchannel becomes increasingly important with the immergence of nano- and micro-electro-mechanical system engineering. In particular, boiling heat transfer is of significant interest for the design of a compact evaporator, which may have extensive applications in industries such as microelectronics, automobile, cryogenics, etc. Recently there have been active researches around the world. For example, Peng and Wang [1], Aligoodarz et al. [2], Zhang et al. [3], Jiang et al. [4], Chen et al. [5], and Lee et al. [6] investigated flow boiling in mini- or microchannels. Although, these previous studies have demonstrated high heat transfer capability of flow boiling in microchannels, the basic heat transfer mechanism is still subject to further investigations. Moreover, there is still lack of model for predicting boiling heat transfer in a microchannel.

Bubble dynamics is fundamental to the understanding and prediction of boiling heat transfer. In a homogeneous medium, the bubble dynamics is governed by the well-known Rayleigh equation or its extended form. Plesset and Zwick [7] and Forster and Zuber [8] have presented elegant solutions for the time evolution of bubble radius. For the very early stage, bubble growth is limited by the inertial force. The bubble grows linearly with time with the proportional constant directly related to the square root of over-pressure divided by liquid density.

* Corresponding author. Tel.: +886 3 5725363; fax: +886 3 5720724.
E-mail address: cpan@ess.nthu.edu.tw (C. Pan).

0017-9310/$ - see front matter © 2004 Elsevier Ltd. All rights reserved.
doi:10.1016/j.ijheatmasstransfer.2004.02.031

Nomenclature

A	cross-section area of channel (m^2)
C_{pl}	specific heat of liquid (J/kg K)
D	bubble departure diameter (μm)
f	bubble frequency (bubbles/s)
G	mass flux (kg/m^2 s)
i_{lv}	latent heat of evaporation (J/kg)
Ja	Jacob number ($\rho_l C_{pl}(T_w - T_{sat})/\rho_v i_{lv}$)
k_l	thermal conductivity of liquid (W/m k)
L	channel length (m)
P	heated perimeter of channel (m)
Pr_l	Prandtl number of liquid
$\dot{Q}_{CH}$	heat transfer rate through microchannel convection or boiling (W)
$\dot{Q}_{IR}$	sensible heat loss to the inlet reservoir (W)
$\dot{Q}_{in}$	total heat input (W)
$\dot{Q}_N$	heat loss due to natural convection from the top side of the test section (W)
$\dot{Q}_{OL}$	other heat losses (W)
$\dot{Q}_R$	radiation heat loss (W)
q''_{ONB}	onset of nucleate boiling heat flux (W/m^2)
q''	heat flux (kW/m^2)
$\dot{R}$	bubble growth rate (μm/ms)
R_D	bubble departure radius (μm)
$r_{c,crit}$	critical cavity radius (m)
$r_{c,max}$	maximum cavity radius (m)
T_w	wall temperature (°C)
T_{surf}	heater surface temperature (°C)
T_{sat}	saturation temperature (°C)
t	time (ms)
$v_{\ell v}$	the specific volume difference between vapor and liquid (m^3/kg)

Greek symbols

ρ_l	the density of liquid (kg/m^3)
ρ_v	the density of vapor (kg/m^3)
ΔP	pressure drop through the channel (Pa)
ΔP_v	pressure difference between vapor in the bubble and surrounding liquid (Pa)
$\Delta T_{sat,ONB}$	onset of nucleate boiling superheat (°C)
α_ℓ	the volume fraction of liquid
σ	surface tension (N/m)

The over-pressure, i.e., the pressure difference between vapor inside the bubble and surrounding liquid, may be related to the liquid superheat through the Clausius–Clapeyron equation. For the latter stage, the bubble is large and its growth requires extensive evaporation from the bubble interface. The latent heat of evaporation is provided by heat diffusion from the liquid nearby the bubble interface. The bubble growth for the latter stage is, therefore, controlled by thermal diffusion and both above solutions indicated that bubble radius is proportional to the square root of time with the proportional constant directly related to the Jacob number.

Bubble growth from a heated wall is much more complicated with the presence of thermal boundary layer near the wall. Prior to the bubble growth, the bubble may stay on a cavity mouth waiting for the establishment of thermal boundary layer such that the liquid temperature at the bubble tip is higher than the vapor temperature inside the bubble [9]. The bubble will then grow rapidly once such a bubble growth criterion is satisfied. The evaporation rate at the bubble interface will be nonuniform: large near the heating wall and small near the bubble tip. Moreover, in an ordinary sized channel, the rapid initial growth of bubble may create a microlayer between the bubble and the heating wall [10]. The evaporation of microlayer has been demonstrated to have a significant effect on bubble growth from a heated wall.

A bubble will depart from the heated wall after it grows to a certain size. For flow boiling in an ordinary sized channel, the major forces acting on a bubble includes buoyancy force, inertial force, surface tension, and drag due to bulk flow in the channel. Surface tension and inertial force tend to retain the bubble to the wall, while the drag and buoyancy forces tend to detach the bubble from the wall. Levy [11] developed a semi-empirical model for bubble departure diameter based on the considerations of buoyancy force, drag due to bulk flow, and surface tension.

The bubble period, and so bubble frequency, may be determined if the waiting time and bubble growth time can be evaluated accurately. The bubble growth time is the intervals from bubble beginning to grow to its departure from the wall. For boiling in an ordinary sized channel, the bubble frequency and departure diameter is usually correlated as fD^n = constant.

Recently, Dhir [12] conducted a review on various aspects of boiling heat transfer including bubble dynamics such as bubble growth, bubble departure and bubble frequency. On the other hand, Kandlikar [13] reviewed some of their works on bubble growth in minichannels. Kennedy et al. [14] investigated the onset of nucleate boiling and onset of flow instability in minichannels. Ghiaasiaan and Chedester [15] examined the applicability of exiting macroscale models on the onset of nucleation boiling in minichannels and proposed a semi-empirical method.

Bubble dynamics in a microchannel may be quite different from that in an ordinary sized channel. Bubble growth in a microchannel is restrained by the channel wall in the transversal direction and experiences a very large pressure gradient, i.e., shear stress in the streamwise direction. Clearly, the bubble size, at least in the transversal directions, is limited by the channel size. With regard to the bubble departure, the buoyancy force is expected to be negligible, while the drag should be very significant due to large pressure drop through the channel. The objective of the present study is to explore experimentally bubble dynamics of boiling in a single microchannel. The bubble dynamics in two parallel microchannels is reported in a companionate paper [16]. Bubble growth rate, bubble departure size and bubble frequency are studied.

2. Experimental details

The experimental setup consists of the test section, a syringe pump, a heating module and a flow visualization system, as shown in Fig. 1(a). The test section is a 5-mm wide silicon stripe, which is made of P-type ⟨100⟩orientation wafer and is etched with the microchannel on its top surface. The test section with the silicon-based

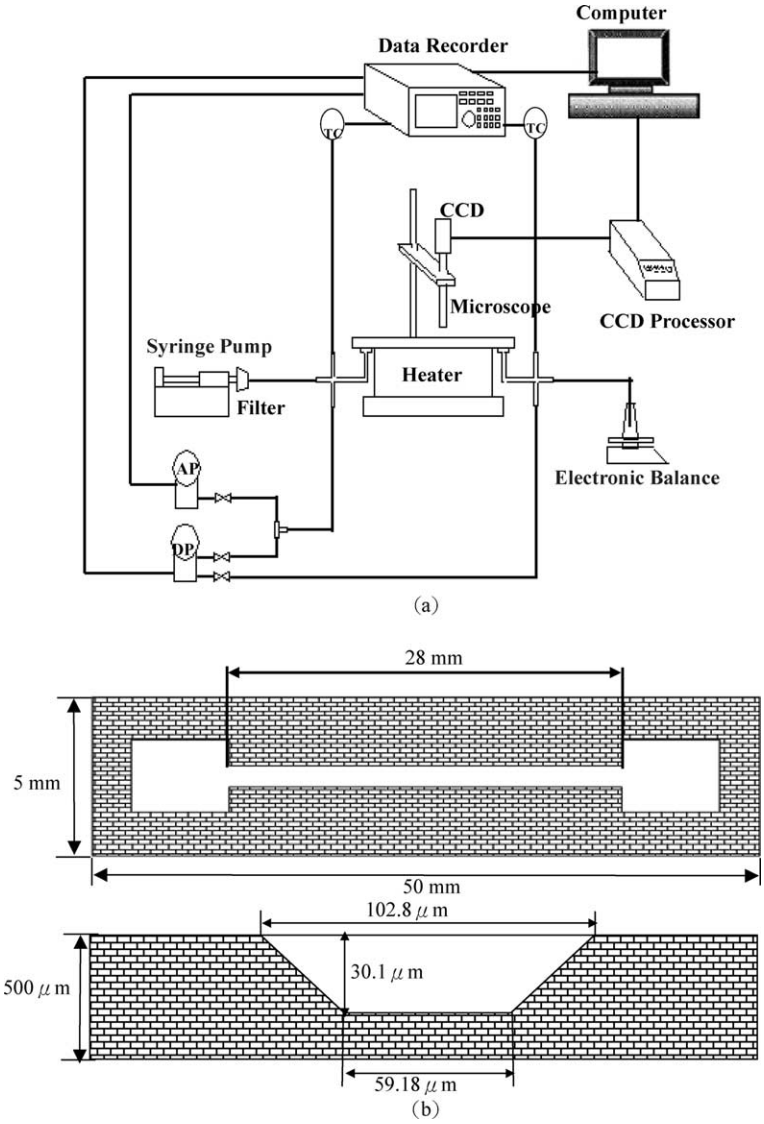

Fig. 1. (a) Schematic of the experimental setup. (b) The top and cross-section views of the test section with a trapezoid microchannel (length shown not in scale).

microchannel is adhered with silver composition (DuPont Electronic, 4817N) on the top of the heating module, which is a copper (C1100, Cu $\geqq$ 99.90, P $\leqq$ 0.004) block heated by a heating element with controllable power. The top surface dimension is 5 mm × 20 mm. Fig. 1(b) displays the top and cross-section views of the test section. The top and bottom widths of the trapezoid channel are 102.8 and 59.12 μm, respectively, and the channel depth is 30.1 μm resulting a hydraulic diameter of 41.3 μm. The channel length is 28 mm leading to a length–diameter ratio of 678. Only the central 20 mm is heated. The dimensions for both inlet and outlet sumps are $3 \times 2\,mm^2$.

The side surfaces of the heating module are insulated with plasters and heat resistance plates. Moreover, to minimize heat loss, the whole heating mode and test section is covered with thick ceramic fiber except the upper portion of the test section to allow for flow visualization.

The fabrication process of the microchannel employs a silicon bulk micromachining and anodic bounding process [6]. The surface roughness of the channel is examined by an atomic force microscope including the section analysis and line profiles. As shown in Fig. 2, the root-mean-square roughness of the bottom surface is 206 nm within an area of 20 μm × 20 μm; while it is 82 nm within an area of 2 μm × 2 μm for the side wall. It can be seen from the surface profiles of Fig. 2 that bumps appear randomly on the surface. The maximum heights of bumps observed for the bottom and side surface are 4.75 and 4.33 μm, respectively.

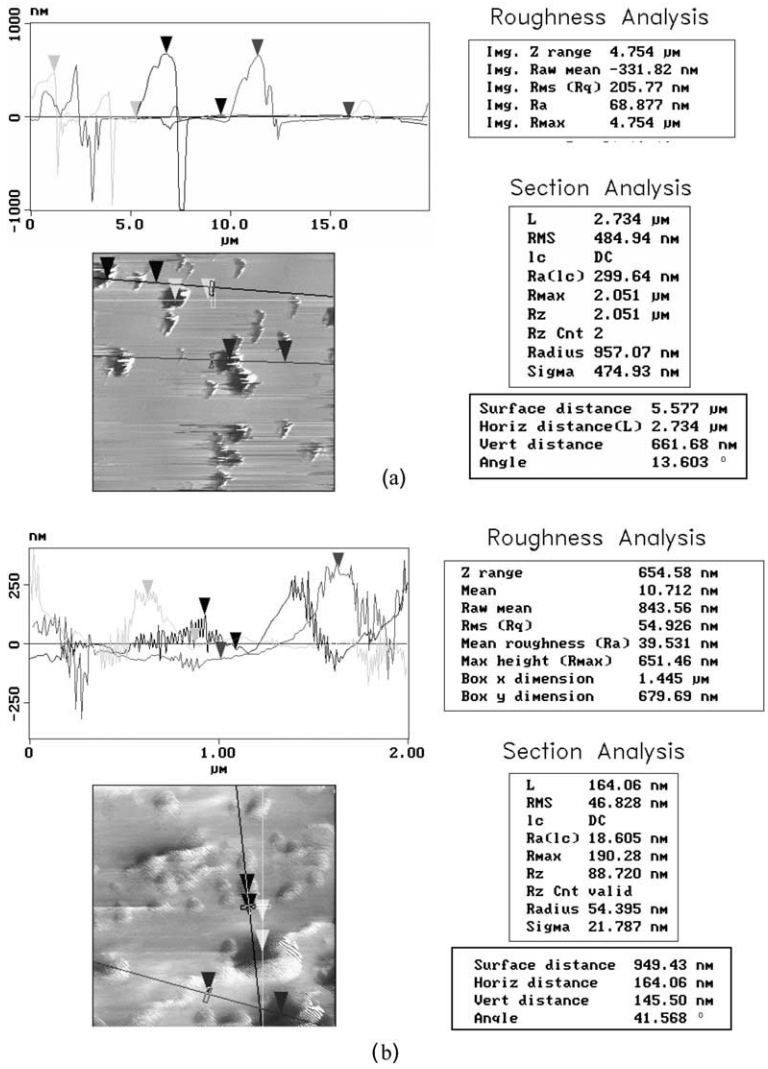

Fig. 2. Surface roughness using an atomic force microscope including section analysis and line profiles: (a) bottom wall and (b) side wall.

The syringe pump provides constant flow of de-ionized water in the microchannel. The flow rate of the pump ranges from 0.001 μl/h to 70.57 ml/min. A Whatman injector filter with a net size of 0.1 μm is installed at the exit of the pump to filter sub-microparticles. An electronic balance, placed at the exit of the loop, provides independent measurement of the mean flow rate. Moreover, it is confirmed that the flow driven by the syringe pump is quite steady based on the weight–time relationship from the electronic balance.

Three K-type thermocouples are embedded 1-mm under the surface of the heating module to measure the surface temperature. The channel wall temperature is then obtained considering the thermal resistance from the location of thermocouple to the bottom wall of the channel. The contact resistance between silicon and copper with the silver composition was measured to be $0.24 \times 10^{-4}\,\mathrm{K\,m^2/W}$ based on the ASTM Standard Test Method D5470-01 [17].

The temperatures at the inlet and outlet reservoirs are measured with a T-type thermocouple inserted into each reservoir. The inlet pressure is measured by a pressure transducer. The outlet pressure is very close to the atmospheric pressure as the channel exit is drained to a container exposed to the atmosphere. Therefore, the variation of inlet pressure also reflects the change of pressure drop through the channel as demonstrated in a previous study [5].

The flow visualization system includes a high-speed digital camera (KODAK motion coder SR-Ultra) and a personal computer. A microlens is mounted on the CCD to observe the two-phase flow pattern in the microchannel. The maximum frame rate of the camera is 10,000 frame/s and the fastest shutter speed is 1/20,000. An x–y–z mechanism is installed with the test module to hold the lens and provide accurate position on the test plane (x–y plane) and focusing (z-direction). The images obtained are analyzed using the Image-Pro to measure the bubble size of each frame. A ruler with each minor division of 65 μm is also etched on the top side of the test section enabling the determination of bubble (center) location and bubble size.

The whole test module, except the syringe pump, was set within an acrylic–plastic case of $50 \times 40 \times 100\,\mathrm{cm^3}$.

2.1. Evaluation of channel wall heat flux and heat loss

The total heat input must be balanced with the heating power to the microchannel and heat losses via various different paths, i.e.,

$$\dot{Q}_{\mathrm{in}} = \dot{Q}_{\mathrm{CH}} + \dot{Q}_{\mathrm{N}} + \dot{Q}_{\mathrm{R}} + \dot{Q}_{\mathrm{IR}} + \dot{Q}_{\mathrm{OL}} \tag{1}$$

The total heat input, $\dot{Q}_{\mathrm{in}}$, can be directly measured experimentally. For the RHS of Eq. (1), $\dot{Q}_{\mathrm{CH}}$ is the heat transfer rate through microchannel convection or boiling, $\dot{Q}_{\mathrm{N}}$ accounts for the heat loss from the glass surface due to natural convection to the air inside the case and may be estimated by a proper correlation; $\dot{Q}_{\mathrm{R}}$ is the radiation heat loss, which can also be evaluated readily given the surface emissivity and temperature of the glass surface and the surroundings; $\dot{Q}_{\mathrm{IR}}$ represents the sensible heat loss to the inlet reservoir due to axial conduction of the test section, which may be determined given the mass flow rate and temperature difference between the inlet reservoir and the injecting tube of the syringe pump;$\dot{Q}_{\mathrm{OL}}$ accounts for other losses including the sensible and latent heat loss to the exit reservoir and possible latent heat loss to the inlet reservoir.

Under single-phase flow conditions, the heat transfer through the microchannel convection may be readily determined from the measurement of mass flow rate and temperature difference between outlet and inlet reservoir. Consequently, the other heat losses during single-phase flow may be determined using Eq. (1), i.e.,

$$\dot{Q}_{\mathrm{OL}} = \dot{Q}_{\mathrm{in}} - \dot{Q}_{\mathrm{CH}} - \dot{Q}_{\mathrm{N}} - \dot{Q}_{\mathrm{R}} - \dot{Q}_{\mathrm{IR}} \tag{2}$$

$\dot{Q}_{\mathrm{OL}}$ is found to increase approximately linearly with heater surface temperature. Such a linear relationship is extrapolated to those temperatures with boiling in the microchannel. Therefore the heat transfer rate through the microchannel boiling can be determined by the following equation:

$$\dot{Q}_{\mathrm{CH}} = \dot{Q}_{\mathrm{in}} - \dot{Q}_{\mathrm{N}} - \dot{Q}_{\mathrm{R}} - \dot{Q}_{\mathrm{IR}} - \dot{Q}_{\mathrm{OL}} \tag{3}$$

The channel wall heat flux can then be obtained by dividing the channel power with the total area of the bottom and two side walls.

2.2. Uncertainty analysis

The uncertainties in temperature measurements are ±0.6 °C and ±1 °C for K- and T-type thermocouples. The uncertainty in flow rate measurements is ±2.9%. The uncertainty in surface heat flux is estimated to be from ±5.94% to ±54.5% with an average value of 19.1%. The highest uncertainty appears for the case with the lowest mass flow rate ($170\,\mathrm{kg/m^2s}$) and heat flux ($1.49\,\mathrm{kW/m^2}$). The heat flux uncertainty generally decreases with increasing heat flux and/or mass flux. The uncertainties in the measurements of instantaneous bubble radius using the Image-Pro are ±3.42% and ±1.47% for spherically and non-spherically growth, respectively.

2.3. Experimental procedure

The present study employs de-ionized water as the working fluid, which is first boiled in a beaker to minimize the dissolved gases in the water. After it is cooled down, the de-ionized water is poured into the injecting tube of the syringe pump. The experiment is started at pumping the fluid into the system at a specific flow rate. The heating power is switched on to a specific level once

the inlet pressure reaches the steady state. This usually takes about 3.5 h. For this study the heating power and thus the heating surface temperature is varied to examine their effects on bubble dynamics in the microchannel at a given flow rate.

3. Results and discussion

3.1. Onset of nucleate boiling

The bubble dynamics studied in the present work is for the bubble at the location of onset of nucleate boiling (ONB) under a given condition. For some situations, bubbles may also be found later in nearby upstream locations. It is found that, in general, at a given flow rate the ONB location moves upstream as the heat flux is increased, as in an ordinary sized channel. For ONB under forced flow conditions (in an ordinary sized channel), the heat flux and wall superheat are related by the following equation if the surface cavities of all sizes are available [18]:

$$q''_{\mathrm{ONB}} = \frac{k_{\mathrm{l}}}{8\sigma v_{\mathrm{lv}} T_{\mathrm{sat}}} \Delta T^2_{\mathrm{sat,ONB}} \tag{4}$$

The bubble will nucleate from the cavity of critical size [19]:

$$r_{\mathrm{c,crit}} = \left(\frac{2\sigma T_{\mathrm{sat}} v_{\mathrm{lv}} k_{\mathrm{l}}}{i_{\mathrm{lv}} q''_{\mathrm{ONB}}} \right)^{1/2} \tag{5}$$

In a microchannel, the surface is usually very smooth, as shown previously in Fig. 2, and the largest cavity available, i.e., $r_{\mathrm{c,max}}$, is very possibly smaller than $r_{\mathrm{c,crit}}$. The ONB will be governed by the following equation [20]:

$$q''_{\mathrm{ONB}} = \frac{k_{\mathrm{l}}}{r_{\mathrm{c,max}}} \Delta T_{\mathrm{sat,ONB}} - \frac{2\sigma k_{\mathrm{l}} T_{\mathrm{sat}} v_{\mathrm{lv}}}{i_{\mathrm{lv}} r^2_{\mathrm{c,max}}} \tag{6}$$

Fig. 3 illustrates a comparison of the data of the present work and prediction of Eq. (6) with various different values of $r_{\mathrm{c,max}}$. For the experimental data points in Fig. 3, the saturation temperature is corresponding to the local pressure at each of the ONB locations. The local pressure is estimated by assuming a linear pressure distribution in the channel between the inlet and out ones. For the evaluation of Eq. (6), the saturation temperature and thermal–physical properties are corresponding to the saturation state of the system pressure, i.e., the arithmetic mean of inlet and outlet pressures. The system pressure may vary from case to case. For Fig. 3 an average system pressure of 161.7 kPa over various different cases of this study is employed. As for the wall temperature, it is assumed that the channel wall temperature is uniform as the channel is relatively short and the wall material–silicon has relatively good thermal conductivity. The figure indicates that most of the cavity sizes

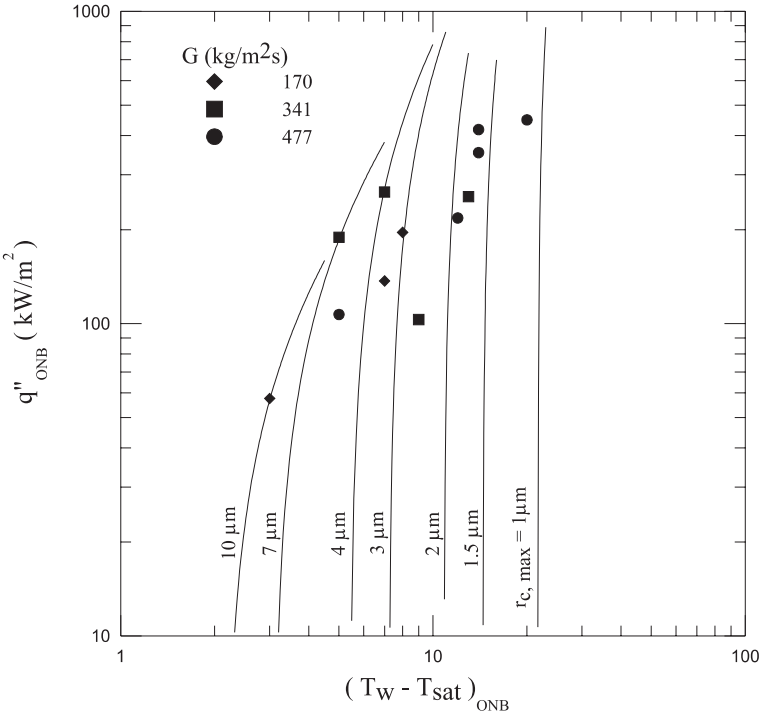

Fig. 3. Relationship between heat flux and wall superheat at the position of incipient boiling.

range from 1.5 to 4 μm. This is consistent with the maximum roughness on the side wall (see Fig. 2).

3.2. Bubble growth

Fig. 4 shows sequential images illustrating a bubble growing at the ONB location for $G = 341\,kg/m^2s$ and $q'' = 189\,kW/m^2$. As stated previously, the ruler etched near the channel helps determination of bubble size and identification of bubble location. For Fig. 4 the bubble nucleates at a site 2.48 mm from inlet. On the same side of the channel another bubble nucleates approximately 65 μm upstream at $t + 10$ ms, while on the other side six more bubbles are also distinctive and growing at the same time. During this early stage, little interactions among bubbles are present. At $t + 70$ ms, the bubble under observation is somewhat distorted and its location is somewhat moved downstream due to the flow effect. At $t + 84.5$ ms, the bubble is actually departing from its nucleation location and the bubble diameter at this moment is defined as the departure diameter. The departure diameter is around 68 μm determined using the edge detection of the Image-Pro. This departure size is actually larger than the channel depth and the bubble growth was actually constrained by both top and bottom walls before departure. This point will

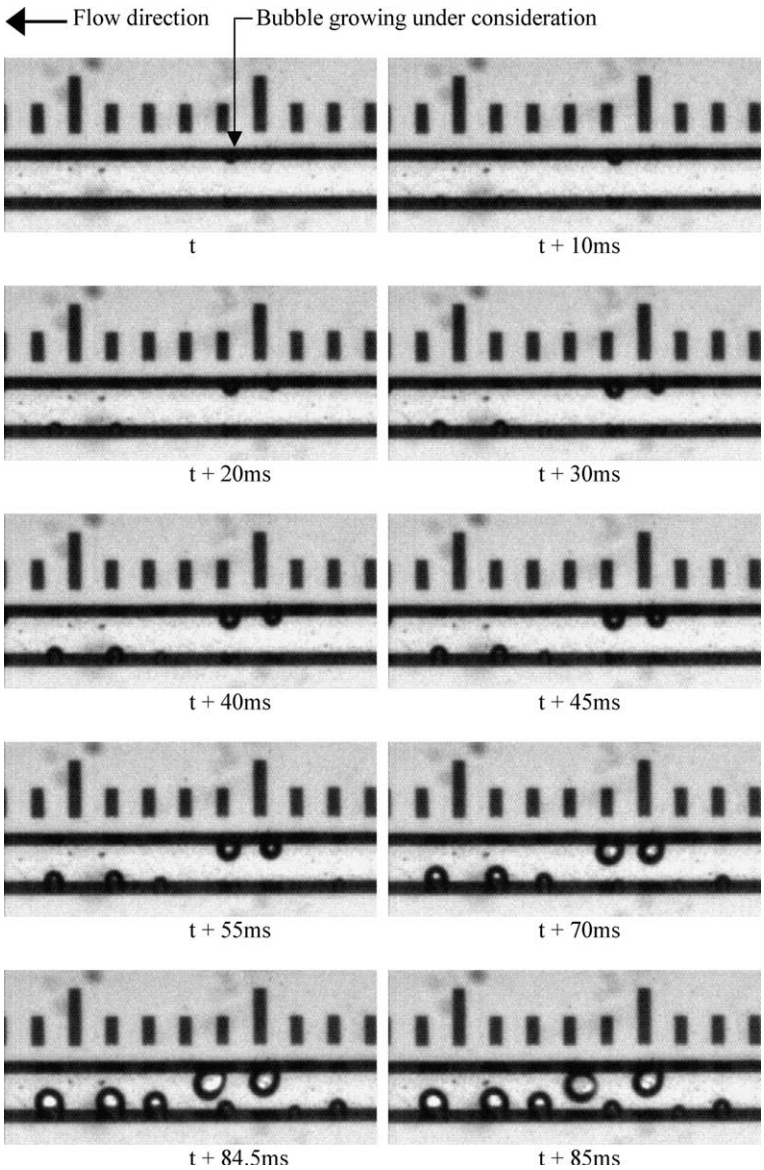

Fig. 4. Sequential images of bubbles growing near the ONB location. From inlet 2.48 mm; $G = 341\,kg/m^2s$; $q'' = 189\,kW/m^2$.

be further discussed in the following paragraph. In total, there are eight active bubbles in the observation window indicating a nucleation site density of 127 bubble/mm^2. It is also interesting to note that all these bubble nucleate from side walls of the channel.

Fig. 5(a) displays the time evolution of bubble radius for this particular site for three consecutive cycles. The open symbols are for the isotropic growth stage that the bubble grows with a spherical shape; while the solid symbols are for the anisotropic growth stage that the bubble has been distorted due to the limitation of channel depth and flow drag. Fig. 5(a) and (b) indicates that the critical radius for the bubble beginning to grow anisotropically is approximately 25–30 μm. At this stage, the bubble diameter is, in fact, larger than the channel depth (30.1 μm) and the bubble has already been limited by the top and bottom walls in the vertical direction. The figure indicates that for this case the bubble grows

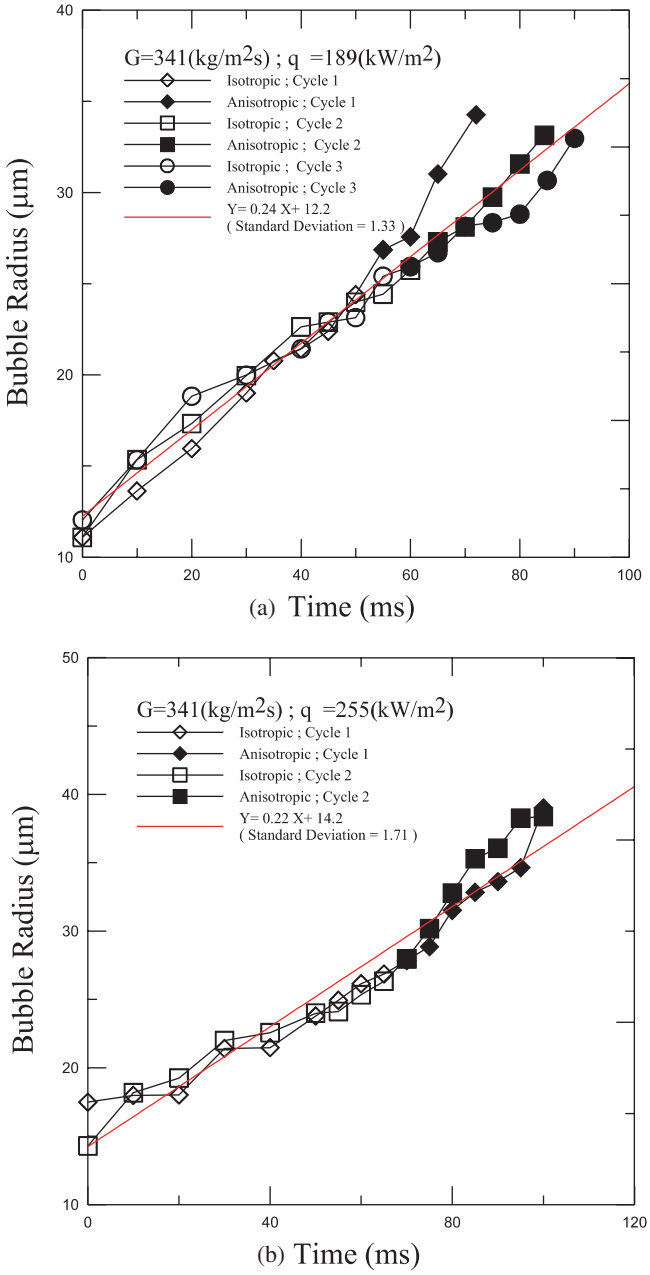

Fig. 5. Time evolution of bubble radius for $G = 341\,\mathrm{kg/m^2s}$: (a) $q'' = 189\,\mathrm{kW/m^2}$ and (b) $q'' = 255\,\mathrm{kW/m^2}$.

quite consistently for these three consecutive cycles except for the period of distorted bubbles, for which the bubble of cycle 2 grows much faster than the other two cycles. During the anisotropic growth period, the bubble growth is significantly affected by the flow drag. The non-uniform bubble growth rate among cycles is not surprising as the local flow field may be changing due to perturbation from various sources such as perturbation from bubbles in other sites. Fig. 5(a) and (b) demonstrate that the bubble grows nearly linearly with time, which is typical in the single microchannel of this study and in the system of two parallel microchannels in Ref. [7].

The linear growth pattern suggests that the bubble growth be inertia controlled. The best fit of the data for Fig. 5(a) gives a growth rate of $0.237 \pm 0.008\,\mu m/ms$ in radius, which is, however, much smaller than that given by the Rayleigh equation, i.e.,

$$\dot{R} = \left[\frac{2}{3}\frac{\Delta P_v}{\rho_\ell}\right]^{1/2} \approx \left[\frac{2}{3}\frac{(T_w - T_{sat})i_{\ell v}}{T_{sat}v_{\ell v}\rho_\ell}\right]^{1/2} = \left[\frac{2}{3}\frac{(128\text{–}123)\ \mathrm{K} \times 2.194 \times 10^6\ \mathrm{J/kg}}{396\ \mathrm{K} \times 0.8205\ \mathrm{m^3/kg} \times 941\ \mathrm{kg/m^3}}\right]^{1/2} = 4.89\ \mathrm{m/s} \quad (7)$$

The Rayleigh equation is for bubble growth in a homogenous, superheated bulk liquid. In a microchannel, the bubble growth is constrained at least in the transversal directions. Moreover, the temperature gradient in the transversal directions is expected to be large and extensive evaporation would occur only in the region very close to the wall. Therefore, a much smaller bubble growth rate than the Rayleigh equation based on wall superheat in the microchannel is reasonable.

For bubble grows on a heated wall with a large thermal conductivity, the Cooper model [21] gives the following equation for transient bubble radius.

$$R(t) = 2.5\frac{Ja}{Pr_1^{1/2}}(\alpha_1 t)^{1/2} \quad (8)$$

where

$$Ja = \frac{\rho_1 C_{pl}(T_w - T_{sat})}{\rho_v i_{lv}} \quad \text{and} \quad Pr_1 = \frac{v_1}{\alpha_1}$$

This equation is based on the evaporation of microlayer underneath the growing bubble. The bubble radius is proportional to the square root of time and is inconsistent with what observed in the present study. This suggests that in the microchannel the microlayer may not be present as in an ordinary sized channel. The images shown in Fig. 4 are not clear enough to confirm the presence or absence of microlayer underneath the growing bubble.

Fig. 6 demonstrates an extraordinarily high bubble growth rate for $G = 341\,kg/m^2s$ and $q'' = 103\,kW/m^2$. The bubble growth rate under this condition is $94.6\,\mu m/ms$ and is much higher than the other cases. For this particular case a much high frame rate of

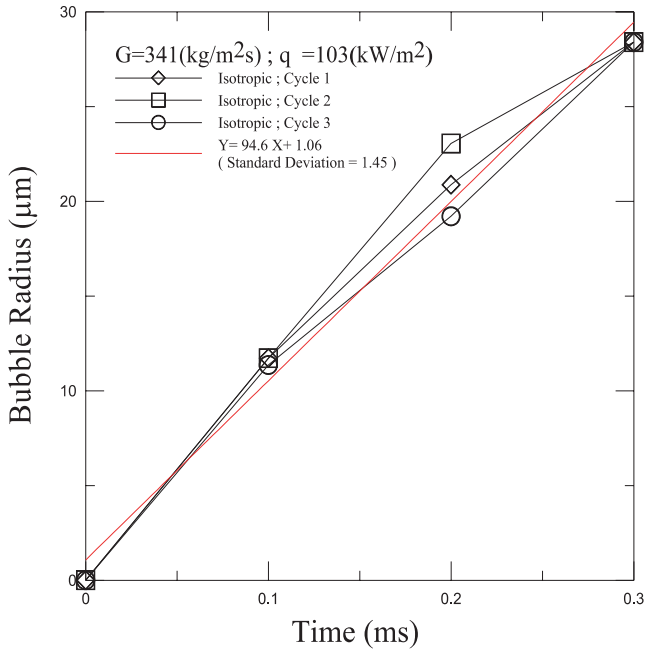

Fig. 6. A case with extraordinarily high bubble growth rate. $G = 341\,kg/m^2s$, $q'' = 103\,W/m^2$.

Table 1
Summary of the effect of mass flux and heat flux on bubble growth rate, initial bubble radius, and bubble departure radius

q'' (kW/m^2)	T_w (°C)	T_{sat} [a] (°C)	$T_{sat,L}$ [b] (°C)	Bubble growth rate (μm/ms)	Initial bubble radius (μm)	Bubble departure diameter (μm)	Remarks
G = 170 (kg/m^2 s)							
1.47 ± 0.80	100	103	103	0.24 ± 0.005	15.1 ± 0.32	45.1	$T_w < T_{sat}$
57.6 ± 20.0	108	105	105	2.62 ± 0.21	12.6 ± 1.38	47.3	
137 ± 23.4	124	112	117	95.3 ± 3.07	21.3 ± 0.40	30.6*	
196 ± 26.9	131	115	123	4.91 ± 0.28	13.4 ± 0.69	27.3*	Reversed flow present
G = 341 (kg/m^2 s)							
6.94 ± 2.13	98	106	107	0.16 ± 0.002	9.74 ± 0.23	33.6	$T_w < T_{sat}$
103 ± 25.3	122	111	113	94.63 ± 3.74	1.06 ± 0.70	28.4*	
189 ± 28.7	128	114	123	0.24 ± 0.008	12.2 ± 0.44	31.1	
264 ± 30.1	134	117	127	0.32 ± 0.02	17.2 ± 0.43	26.9	
255 ± 31.9	145	119	132	0.22 ± 0.01	14.2 ± 0.66	38.7	Reversed flow present
G = 477 (kg/m^2 s)							
15.7 ± 1.87	100	108	108	0.19 ± 0.003	5.56 ± 0.29	40	$T_w < T_{sat}$
107 ± 18.5	116	109	111	7.09 ± 0.492	1.90 ± 1.43	36.4	
218 ± 21.1	130	114	118	72.8 ± 9.15	20.5 ± 1.18	29.9*	
353 ± 24.3	144	120	130	0.54 ± 0.036	13.1 ± 1.18	38.9	
415 ± 25.9	150	123	136	0.10 ± 0.01	17.9 ± 1.07	47	
449 ± 26.7	157	124	137	0.10 ± 0.01	14.1 ± 0.67	19.2	Reversed flow present

*10,000FPS.
[a] Corresponding to system pressure = (P_{in} + 1 atm)/2.
[b] Corresponding to local pressure at the nucleate boiling location based on linear pressure distribution in the channel.

10,000 frame/s was employed in the experiment. It is unclear why the bubble growth rate for such a case is much higher than the other cases.

Table 1 summarizes the effect of mass flux and heat flux on bubble growth rate. The bubble growth rates range from 0.12 to 7.09 μm/ms, except for the three cases with extraordinarily high growth rates. At the low heat flux region, the bubble growth rate increases with increase in heat flux as expected. Extensive evaporation at high heat fluxes results in a larger growth rate than at low heat fluxes. As the heat flux does, the mass flux also has a significant effect on the bubble growth rate. In general, the bubble grows faster at low flow rates than at high flow rates. This is because high evaporation rates at low mass fluxes. Indeed, under saturated conditions, the vapor quality gradient in the axial direction is proportional to the heat flux but inversely proportional to the mass flux as

$$\frac{dx}{dz} = \frac{q''P}{GAi_{lv}} \tag{9}$$

At the high heat flux region, however, the bubble growth rate decreases with increase in heat flux. This reversed trend may be due to the movement of the ONB location toward upstream, at which the pressure and water temperature is close to at the inlet, as the heat flux is increased. The local saturation temperature corresponding to the local pressure is elevated as the heat flux is increased (see Table 1). The increase of local pressure and saturation temperature may suppress the growth of the bubble.

As for the case of $G = 341\,kg/m^2s$ and $q'' = 103\,kW/m^2$, the bubble growth rates for the cases of $G = 170\,kg/m^2s$, $q'' = 137\,kW/m^2$ and $G = 477\,kg/m^2s$, $q'' = 218\,kW/m^2$ are extraordinarily high. For these three cases, the growth rates are from 72.8 to 95.3 μm/ms, which are two orders of magnitude higher than the other cases.

Significantly, for the case with the least mass flux, i.e., $G = 170\,kg/m^2s$, a constant bubble growth rate is only a rough approximation. At least for $q'' = 57.6\,kW/m^2$ and $196\,kW/m^2$, the bubble grows faster and faster, approaching an exponential growth, especially during anisotropic growth (see Fig. 7). This is somewhat unusual. As discussed previously, for the anisotropic growth stage, the bubble diameter is actually larger than the channel depth and is thus constrained by the top and bottom walls. The bubble can only grow in the other two directions. The same evaporation rate may results in a larger growth rate viewed from the top side as in the present study. On the other hand, the pressure field around the bubble may be momentarily low at the latter stage of bubble growth. The flow is unstable for the case of $G = 170\,kg/m^2s$, $q'' = 196\,kW/m^2$ as remarked in Table 1.

For the cases of $G = 170\,kg/m^2s$, $q'' = 1.47\,kW/m^2$; $G = 341\,kg/m^2s$, $q'' = 6.94\,kW/m^2$; $G = 477\,kg/m^2s$, $q'' =$

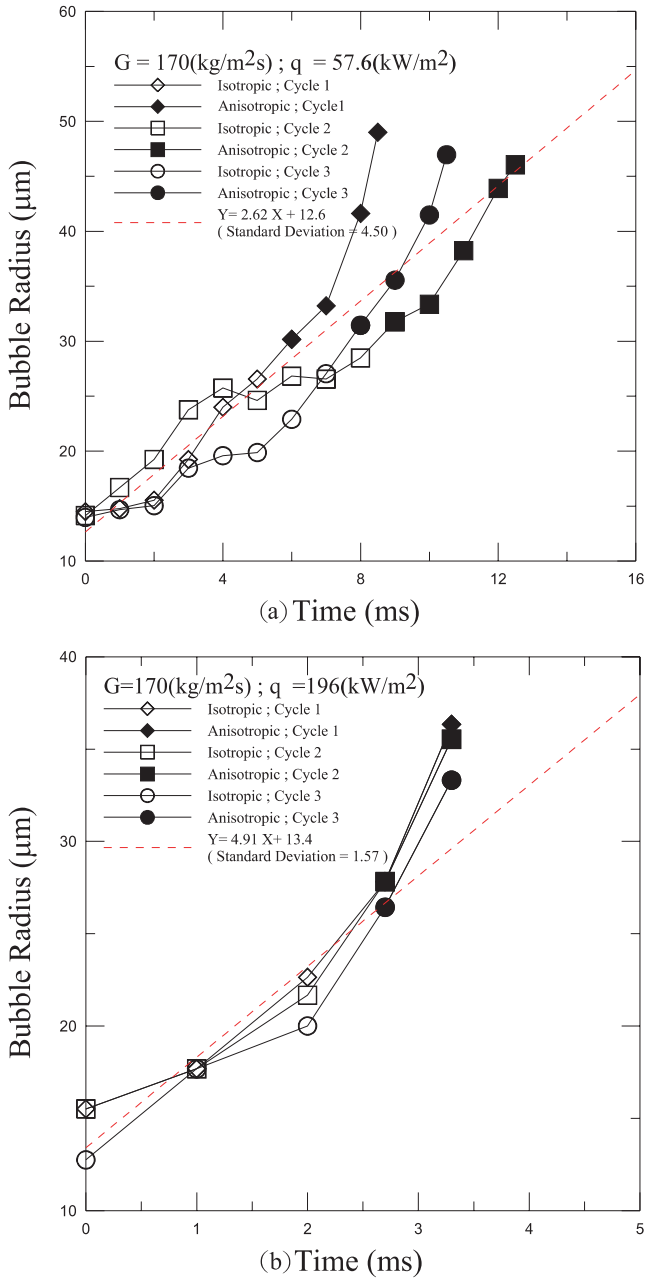

Fig. 7. Unusual bubble growth for $G = 170\,\mathrm{kg/m^2 s}$: (a) $q'' = 57.6\,\mathrm{kW/m^2 s}$ and (b) $q'' = 196\,\mathrm{kW/m^2}$.

15.7 kW/m^2, the heater surface temperature is lower than the saturation temperature corresponding to the atmospheric pressure. The bubble may be nucleated due to dissolved gases. For these cases, the bubble also grows at a constant rate.

Table 1 also lists the initial bubble radius, i.e., the radius at $t = 0$, which may be considered as the size of the bubble sitting on heating surface waiting for growth. Table 1 shows that the initial bubble radius generally are from 10 to 18 μm.

The above results on bubble growth demonstrate that the experimental data are quite scattering and cannot be consistent explained by the existing models. Indeed, bubble growth from a heated wall is very complicated as commented by Dhir in his recent review on boiling heat transfer [12]: "After three decades of research, we

still do not have an effective, consistent model for bubble growth on a heated surface that appropriately includes microlayer contribution and time-varying temperature and flow field around the bubble." Hsu and Graham [22] also commented that on his text book on boiling heat transfer "...any attempt to compare the analyses against growth rate of specific individual bubble is futile. It is as impossible as trying to predict the growth rate of a particular boy using a universal equation." Hopefully, the data presented in the present work may help developing a model for the mean bubble growth rate in microchannels.

3.3. Bubble departure size

Fig. 8(a) shows the effect of heat flux and mass flux on bubble departure radius. Table 1 also lists the bubble departure radius for various different cases of this study.

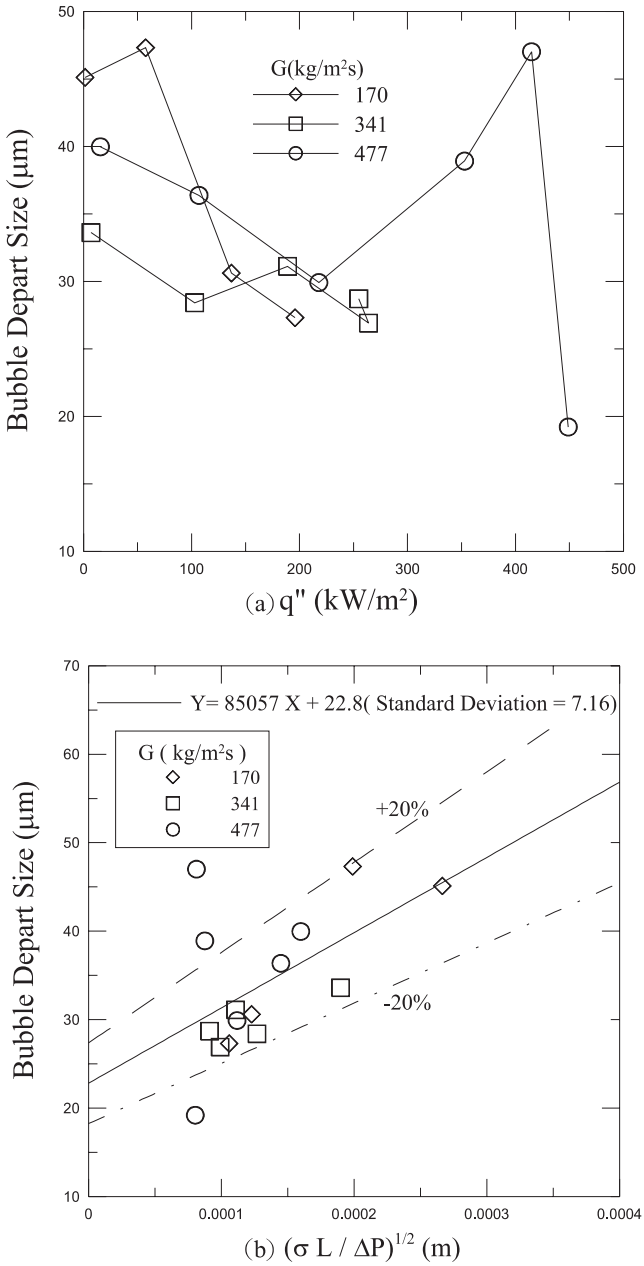

Fig. 8. (a) The effect of heat flux on bubble departure radius and (b) a correlation for bubble departure radius.

In general, the bubble departure radius decreases with increase in heat flux. It should be noted that the bubble under study is at the location of ONB, which moves toward upstream as the heat flux is increased. The mass flux, however, has a mixed effect on bubble departure radius. For low heat fluxes, the bubble departure size for the lowest mass flux ($G = 170\,\mathrm{kg/m^2 s}$) is the largest for the three flow rates under study; while the bubble departure radius for $G = 341\,\mathrm{kg/m^2 s}$ is smaller than that for $G = 477\,\mathrm{kg/m^2 s}$. In a microchannel, the buoyancy force may be considered to have a negligible effect on bubble departure size. Since the bubble grows relatively slowly, the inertial force is also expected to be small. Consequently, surface tension and the drag due to bulk flow will be the dominant forces influencing the bubble departure size. Following an approach similar to Levy's

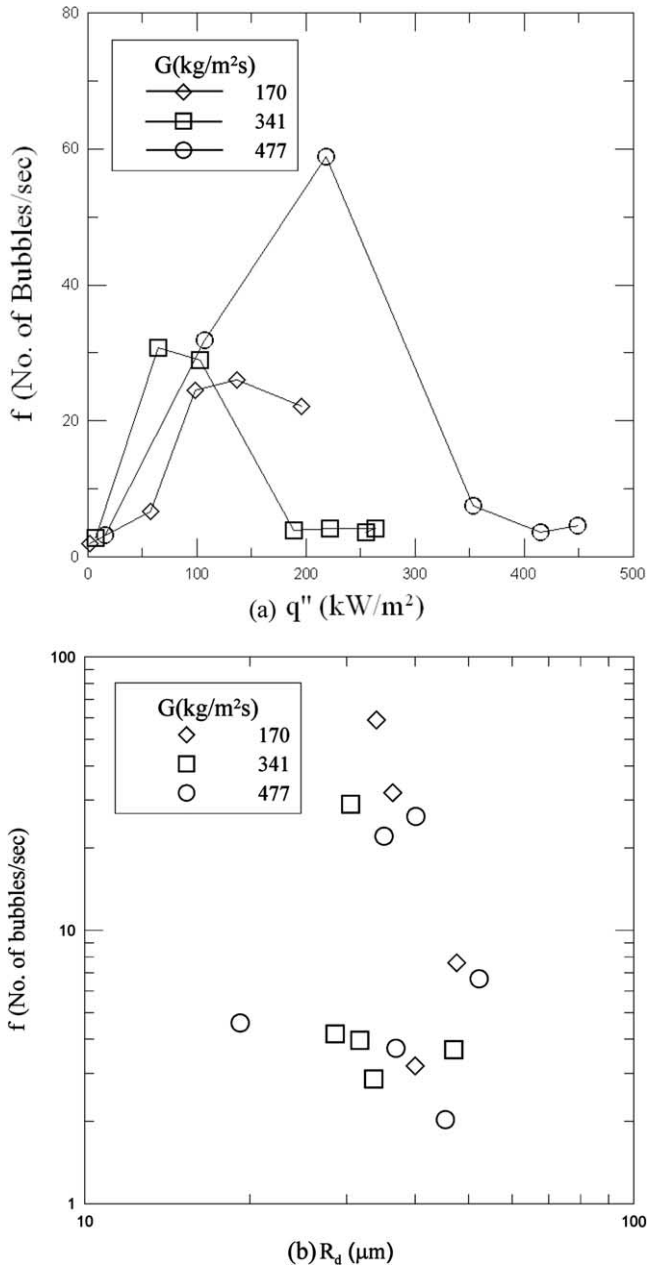

Fig. 9. (a) Bubble frequency at ONB location corresponding to various heat fluxes. (b) Bubble frequency at ONB location relative to each bubble departure radius.

model [11], the bubble departure radius may be correlated as:

$$R_D = C_1 \left[\frac{\sigma}{-\frac{dp}{dz}} \right]^{1/2} + C_2 \simeq C_1 \left(\frac{\sigma L}{\Delta P} \right)^{1/2} + C_2 \qquad (10)$$

where R_D is the bubble departure radius (μm), σ is the surface tension, L is the channel length and ΔP is the pressure drop through the channel. Here, the local pressure gradient has been approximated by the pressure drop through the channel divided by the channel length. The best fit of data against above equation gives $C_1 = 8.51 \times 10^4$, $C_2 = 22.8$. Fig. 8(b) shows that 80% of the data points can be predicted by the correlation within ±20%.

3.4. Bubble departure frequency

Detailed model of nucleate boiling heat transfer requires information of bubble departure diameter as well as departure frequency. Fig. 9(a) illustrates the effect of heat flux and mass flux on bubble frequency. Notably, the location of bubble observed moves toward upstream as the heat flux is increased. The bubble frequency increases very rapidly with increase in heat flux initially. For low mass fluxes, i.e., $G = 170$ and $341\,kg/m^2s$ the bubble frequency quickly rises to about 30 bubbles/s at $q'' \approx 50$–$70\,kW/m^2$. For $G = 477\,kg/m^2s$, the bubble frequency rises to about 60 bubbles/s initially. Such a bubble frequency is comparable to that in an ordinary sized channel. The bubble frequency begins to fall significantly as the heat flux is further increased. This may be due to the fact that for high heat fluxes the bubbles observed are very close to the inlet, at which the bulk liquid temperature is relatively low compared to the local saturation temperature and the local superheat is, in fact, very low.

The bubble frequency is traditionally correlated with bubble departure diameter with a form of $fD^n = $ constant. Fig. 9(b) illustrates that in the microchannel of this study the bubble departure radius varies in a narrow range of 25–50 μm due to the constrain of the channel, while the bubble frequency changes quite significantly from 2 to 60 bubbles/s. A correlation of the tradition form seems to be inexistent.

4. Summary and conclusions

Bubble dynamics for convective boiling in a single microchannel is studied experimentally in the present work. Bubble growth in the microchannel is investigated using a high speed digital camera mounted with a microlens. The images obtained are analyzed using Image-Pro to measure the time evolution of bubble size. The following conclusions may be drawn from the results of the study:

1. The bubble nucleation in the trapezoidal microchannel of this study may be predicted by the classical model with microsized cavities and the bubble typically grows with a constant rate indicating its growth is inertia controlled. Possibly due to space restrain and significant temperature gradient in the transversal directions, the bubble growth rate is much smaller than that predicted by the Rayleigh equation.
2. The size of bubble departure from the microchannel wall is found to be governed by surface tension and drag of bulk flow and may be fairly correlated by a modified form of Levy equation.
3. Bubble frequency in the microchannel is comparable to that in an ordinary sized channel. However, the tradition form of frequency–departure diameter relationship seems to be inexistent in the microchannels of this study.

Acknowledgments

This work was supported by the National Science Council of Taiwan, ROC, under the contract of NSC-90-2212-E-007-103. The authors would like to express their appreciation to Mr. J.H. Hwang and Mr. C.T. Lu for their excellent work in the measurement of contact thermal resistance. The apparatus was provided by Prof. W.K. Lin of the authors' Department, which is also highly appreciated.

References

[1] X.F. Peng, B.X. Wang, Forced-convection and flow boiling heat transfer for liquid flow through micro-channels, Int. J. Heat Mass Transfer 36 (1993) 3421–3427.
[2] M.R. Aligoodarz, Y. Yan, D.B.R. Kenning, Wall temperature and pressure variations during flow boiling in narrow channels, in: Heat Transfer 1998, Proceedings of 11th IHTC, vol. 2, 1998, pp. 225–230.
[3] L. Zhang, J.M. Koo, L. Jiang, S.S. Benerjee, M. Ashegi, K.E. Goodson, J.G. Santiago, T.W. Kenny, Measurements and modeling of two-phase flow in micro-channels with nearly-constant heat flux boundary conditions, in: Proceeding of Micro-Electro-Mechanical Systems (MEMS)-2000, 2000, pp. 129–135.
[4] L. Jiang, M. Wong, Y. Zohar, Forced convection boiling in a micro-channel heat sink, J. Micro-electro-mechanical Syst. 10 (2001) 80–87.
[5] W.L. Chen, F.G. Tseng, C. Pan, Boiling heat transfer and pressure drop in silicon-based micro-channels, in: Proceedings of Pacific Rim Workshop on Transducers and Micro/Nano Technologies, Xiammen, China, 2002, pp. 307–310.
[6] P.C. Lee, H.Y. Li, F.G. Tseng, C. Pan, Nucleate boiling heat transfer in silicon-based microchannel, in: Proceeding of ASME Summer Heat Transfer Conference, Las Vegas, Nevada, USA, 2003.

[7] M.S. Plesset, S.A. Zwick, Growth of vapor bubbles in superheated liquids, Appl. Phys. 25 (1954) 493–500.
[8] H.K. Forster, N. Zuber, Growth of a vapor bubbles in superheated liquid, Appl. Phys. 25 (1954) 474–478.
[9] Y.Y. Hsu, On the size range of active nucleation cavities on a heating surface, J. Heat Transfer 84 (1962) 207–216.
[10] F.D. Moore, R.B. Mesler, The measurement of rapid surface temperature fluctuations during nucleate boiling of water, AIChE J. 7 (1961) 620–624.
[11] S. Levy, Forced convection subcooled boiling prediction of vapor volumetric fraction, Int. J. Heat Mass Transfer 10 (1967) 951–965.
[12] V.K. Dhir, Boiling heat transfer, Annu. Rev. Fluid Mech. 30 (1998) 365–401.
[13] S.G. Kandlikar, Fundamental issue related to flow boiling in minichannel and microchannels, Exp. Thermal Fluid Sci. 26 (2002) 389–407.
[14] J.E. Kennedy, G.M. Roach Jr., M.F Dowling, S.I. Abdelkhalik, S.M. Ghiaasiaan, S.M. Jete, Z.H. Quershi, The onset of flow instability in uniformly heated horizontal microchannels, J. Heat Transfer 122 (2000) 118–125.
[15] S.M. Ghiaasiaan, R.C. Chedester, Boiling incipience in microchannels, Int. J. Heat Mass Transfer 45 (2002) 4599–4606.
[16] H.Y. Li, F.G. Tseng, Chin Pan, Bubble dynamics in microchannels (II) two parallel microchannels, Int. J. Heat Mass Transfer, submitted for consideration.
[17] ASTM International, Standard teat method for thermal transmission properties of thin thermally conductive solid electrical insulation material, D5470-01.
[18] T. Sato, H. Matsumura, On the conditions of incipient subcooled boiling and forced convection, Bull. Jpn. Sci. Mech. Eng. 7 (1963) 392–398.
[19] J.G. Collier, J.R. Thome, Convective Boiling and Condensation, third ed., Clarendon Press, Oxford, UK, 1994, 191.
[20] R. Hino, T. Ueda, Studies on heat transfer and flow characteristics in subcooling flow boiling—part 1 boiling characteristics, Int. J. Multiphase Flow 11 (1985) 269–281.
[21] M.G. Cooper, The microlayer and bubble growth in nucleate pool boiling, Int. J. Heat Mass Transfer 12 (1969) 915–933.
[22] Y.Y. Hsu, R.W. Graham, Transport Processes in Boiling and Two-phase System Including Near-critical Fluids, American Nuclear Society, La Grange Park, IL, USA, 1987, 29.